Check for updates

Particle & Particle Systems Characterization
www.particle-journal.com

Photoinduced Toxicity Caused by Gold Nanozymes and Photodynamic Dye Encapsulated in Submicron Polymer Shell

Igor S. Sergeev, Elizaveta A. Maksimova, Ekaterina O. Moiseeva, Olga Yu. Griaznova, Sergei A. Perkov, Polina A. Demina, Valeriy D. Zaytsev, Yury A. Koksharov, Maxim A. Rider, Ilya A. Zavidovskiy, Polina G. Rudakovskaya, Roman I. Romanov, Boris N. Khlebtsov, Anna O. Orlova, Sergey M. Deyev, and Dmitry A. Gorin*

The development of nanozymes, artificial enzymes made from inorganic nanoparticles, is widely studied due to their affordability, durability, and strength. Gold nanoparticles (AuNPs) are employed to imitate peroxidase, glucose oxidase, lactate oxidase, superoxide dismutase, and catalase. The last one transforms intracellular hydrogen peroxide into molecular oxygen, whose deficiency is characteristic of the hypoxic tumor microenvironment. Thus, gold nanoparticles are thought to enhance the overall effectiveness of photodynamic therapy. However, the enzyme-like activity of nanoparticles rapidly decreases in biological media, due to the aggregation and formation of the so-called "protein corona". In this study, polymeric submicrocapsules loaded with AuNPs and a photodynamic dye are fabricated via Layer-by-Layer (LbL) assembly. The enhancement of photodynamic treatment efficacy by in situ production of oxygen by the catalase-like effect of AuNPs is investigated. Polymeric capsules are thoroughly characterized in terms of physicochemical and catalytic properties, and as a proof of concept, their therapeutic potential is evaluated in vitro. Furthermore, encapsulated AuNPs shows significantly lower aggregation both upon storage and during the reaction course. The results shows that the polymer capsules, containing AuNPs and photodynamic dye, show significantly higher light-induced cytotoxicity in comparison to the individual photodynamic dye, suggesting a synergistic effect between the formation of molecular oxygen by catalase-like gold nanozymes and photodynamic action.

1. Introduction

Photodynamic therapy (PDT) is a relatively recently developed but still one of the most promising cancer treatment methods due to its overall lower toxicity and minimal invasiveness compared to other existing methods.[1,2] Normally, PDT involves the administration of a photosensitizing agent followed by its activation by light at a specific wavelength. In the presence of oxygen, the photochemical reaction aids in the overproduction of highly reactive singlet oxygen or other reactive oxygen species (ROS) that subsequently leads to cell death.[3] However, the efficiency of PDT is severely diminished by the hypoxic tumor microenvironment (TME).[4,5] One of the strategies to overcome this limitation is in situ production of oxygen through the decomposition of intratumoral H_2O_2.[6]

In biological systems, the decomposition of hydrogen peroxide to water and oxygen is accelerated by catalase. This enzyme is normally part of the antioxidant defense machinery that protects cells from damage by oxidative stress.[7] Oxidative stress is induced by the overexpression

I. S. Sergeev, E. A. Maksimova, E. O. Moiseeva, O. Y. Griaznova, S. A. Perkov, V. D. Zaytsev, P. G. Rudakovskaya, D. A. Gorin
Center for Photonic Science and Engineering
Skolkovo Institute of Science and Technology
Moscow 121205, Russia
E-mail: igor.sergeev@skoltech.ru

I. S. Sergeev, P. A. Demina
FSRC "Crystallography and Photonics" RAS
Moscow 119333, Russia

E. O. Moiseeva
Faculty of Chemistry
M.V.Lomonosov Moscow State University
Moscow 119991, Russia

O. Y. Griaznova, P. A. Demina, S. M. Deyev
Shemyakin-Ovchinnikov Institute of Bioorganic Chemistry RAS
Moscow 117997, Russia

O. Y. Griaznova, S. M. Deyev
National Research Nuclear University MEPhI (Moscow Engineering Physics Institute)
Moscow 115409, Russia

P. A. Demina
Moscow Pedagogical State University (MPGU)
Moscow 119991, Russia

The ORCID identification number(s) for the author(s) of this article can be found under https://doi.org/10.1002/ppsc.202300149

DOI: 10.1002/ppsc.202300149

 © 2024 Wiley-VCH GmbH

of ROS, which comprise both free radical (hydroxyl radicals and superoxide radicals) and non-radical (molecular) forms (singlet oxygen and hydrogen peroxide). In the case of low antioxidant levels, ROS imbalance can cause DNA damage resulting in inflammation or even more serious diseases such as cancer or diabetes.[8] However, catalase can also be employed in cancer cells for a sufficient oxygen supply during PDT. Therefore, the integration of nanostructures that mimic catalase-like activity is considered to improve the total efficacy of PDT treatment.[9]

The design of artificial enzymes based on inorganic nanoparticles, also known as nanozymes, has received a significant amount of attention due to their low cost, stability, and robustness.[10,11] To date, nanozymes have been developed for different demands, including cancer therapy, antibacterial therapy, chemodynamic therapy, biosensing, and even environmental protection.[12–14]

During rapid discoveries in nanotechnology, gold nanoparticles (AuNPs) have emerged as promising materials with various applications owning to their unique electronic,[15] optical,[16] and catalytic[17] properties. As with any other heterogeneous catalysts, AuNPs exhibit morphology- and size-dependent properties and can thus be tuned precisely to achieve the optimal characteristics for the best catalytic performance. Previously, gold nanoparticles have been employed as an efficient catalyst for hydrogenation of different organic substrates,[18] CO oxidation at room temperature,[19] as well as enzyme mimic. Due to the biocompatibility of gold nanoparticles, they have been used to mimic catalase,[20] peroxidase,[21] glucose, and lactate oxidase,[12] and superoxide dismutase.[22] Interestingly, the pH dependence of catalytic activity has been previously described for the decomposition of hydrogen peroxide by gold nanoparticles: hydroxyl radicals have been generated at lower pH (peroxidase-like activity), while a higher pH was required for the generation of molecular oxygen (catalase-like activity).[23] The generally accepted mechanism includes four steps (Equations (1)– (4)).[24] As a first step, H_2O_2 is adsorbed on AuNPs forming $Au(H_2O_2)$ surface-active sites. Then adsorbed hydrogen peroxide accepts an electron from the gold metal and decomposes into OH^- ions and $OH^{\cdot}$ radicals. The hydroxide ion OH^- can reacts with free H_2O_2 to yield the hydroperoxyl anion HO_2^- and water. Last, hydroperoxyl anion HO_2^- oxidizes with adsorbed OH radical with formation of O_2 and another water molecule, regenerating Au.

$$Au + H_2O_2 \rightarrow Au(H_2O_2) \quad (1)$$

$$H_2O_2 + e^- \rightarrow OH^- + OH^{\cdot} \quad (2)$$

$$H_2O_2 + OH^- \rightarrow HO_2^- + H_2O \quad (3)$$

$$Au(OH^{\cdot}) + HO_2^- \rightarrow Au + O_2 + H_2O \quad (4)$$

Electrostatically stabilized gold nanoparticles are typically used to achieve high catalase-like activity.[23,25] Despite the good performance in the model reactions, the activity of nanoparticles often rapidly decreases in biological media. The main reasons for that are its aggregation in biological fluids of high ionic strengths, resulting in a reduced surface area[26] and the formation of the so-called "protein corona" caused by the high content of biomacromolecules, including lipids, polysaccharides, nucleic acids, and, especially, proteins that are adsorbed on the surface of nanoparticles.[27] The protein corona alternates both the surface chemistry and hydrodynamic properties of nanoparticles.[28] Changes in the shell composition and zeta-potential in the case of electrostatically stabilized particles affect not only their biodistribution and circulation lifetime but also, most importantly, their catalytic activity. There are two main approaches commonly used to overcome these challenges. The most widely used strategy is based on steric stabilization provided by polymers such as polyethylene glycol covalently attached to the particle surface.[29] However, these particles have been reported to exhibit significantly lower catalytic activity compared to electrostatically stabilized gold nanoparticles.[30] Another method is protein surface coating that has emerged as an outstanding protection for ultrasmall (<2 nm) nanozymes.[31] Nevertheless, because of various limitations in therapeutic applications and the low level of fundamental knowledge, the functional design of nanozymes minimizing the trade-off between stability and catalytic activity remains a big challenge in nanotechnology today.

The inverse dependence of catalytic activity on nanoparticle size is a well-known rule in colloidal chemistry due to the higher surface-to-volume atoms ratio.[32] In addition to that, 3 nm-sized AuNPs have been shown to possess a good cellular uptake[33] and low cytotoxicity.[34] However, despite the fact that its small size leads to comparatively faster clearance from blood by macrophage uptake[35] they can also penetrate the brain-blood barrier (BBB).[36]

One of the possibilities to increase the circulation lifetime is the encapsulation of AuNPs. The use of polymer capsules usually decreases their cytotoxicity[37] and at the same time protects them from the environment, which in the case of nanoparticles prevents their aggregation while conserving their high catalytic activity.[38] These polymer capsules are usually manufactured via a layer-by-layer (LbL) approach. It consists of the sequential deposition of oppositely charged polyelectrolytes on a colloidal template, which is subsequently removed.[39] Due to the versatility of this process, it is possible not only to encapsulate inorganic nanoparticles within such carriers but also to combine them with various organic molecules such as drugs and even photodynamic dyes loaded inside or between layers.[40,41] Because of the selective permeability of the polymeric shell, these capsules can serve as nano- or microreactors where the active compounds are confined inside the capsule, while as small molecules substrates and products can be continuously transferred through the shell. Previously, antioxidant microcapsules with manganese dioxide nanoparticles were manufactured using the LbL approach and reduction of oxidative stress has been shown in vitro.[39] Other

Y. A. Koksharov
Faculty of Physics
M.V.Lomonosov Moscow State University
Moscow 119991, Russia
M. A. Rider, A. O. Orlova
ITMO University
Saint Petersburg 197101, Russia
I. A. Zavidovskiy, R. I. Romanov
Moscow Institute of Physics and Technology
Dolgoprudny 141701, Russia
B. N. Khlebtsov
Institute of Biochemistry and Physiology of Plants and Microorganisms
Russian Academy of Sciences
Saratov 410049, Russia

© 2024 Wiley-VCH GmbH

15214117, 2024, 5, Downloaded from https://onlinelibrary.wiley.com/doi/10.1002/ppsc.202300149 by ITMO University, Wiley Online Library on [17/07/2024]. See the Terms and Conditions (https://onlinelibrary.wiley.com/terms-and-conditions) on Wiley Online Library for rules of use; OA articles are governed by the applicable Creative Commons License

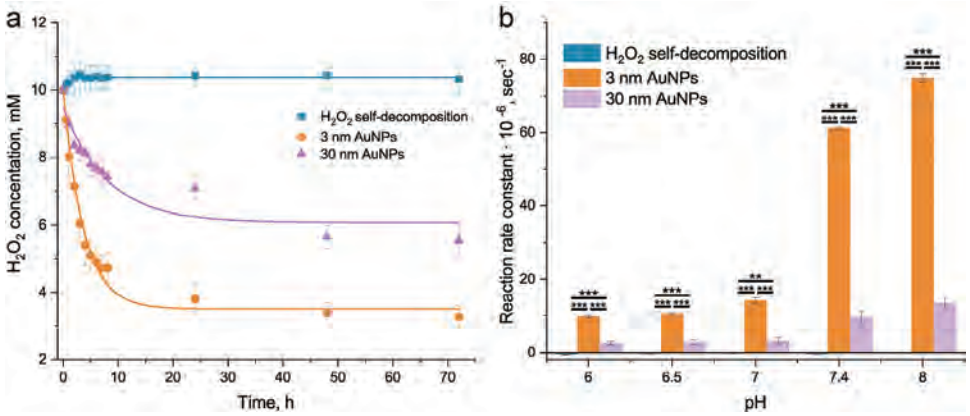

Figure 1. a) Kinetic curves of H_2O_2 self-decomposition and decomposition under the influence of gold nanoparticles of different size at pH = 7.4. Lines represent exponential fit. Error bars represent the SD (n = 3); b) Reaction rate constant dependence on pH of the reaction medium. All samples were normalized to gold concentration, 10 μgml^{-1}. Error bars represent the SD (n = 3). A statistically significant difference is indicated by ** at $P < 0.001$ and *** at $P < 0.0001$, obtained using a two-level ANOVA.

examples of using polymer capsules as reaction compartments include loading of catalase to prevent oxidative stress[42] and the use of cerium oxide nanoparticles as a protective shell for an encapsulated enzyme.[43]

In this study, we compared AuNPs of two different sizes and investigated the improvement of the efficacy of photodynamic treatment by in situ production of oxygen to overcome tumor hypoxia limitations. We prepared polymeric submicrocapsules loaded with gold nanoparticles and Photosens photodynamic dye via LbL assembly. The capsules containing ultrasmall gold nanoparticles and phthalocyanine photosensitizer were thoroughly characterized in terms of physico-chemical and catalytic properties and, as a proof of concept, their therapeutic potential was evaluated in vitro. The polymer capsules showed significantly lower aggregation of nanoparticles upon storage and reaction course. The incorporation of gold nanoparticles was proved to increase the cell toxicity of photodynamic agent as a result of oxygen generation from overproduced intracellular hydrogen peroxide. A light-induced catalytic microreactor represents an important step toward the development of efficient therapeutic PDT agents and opens up new cancer treatment opportunities.

2. Results and Discussion

2.1. Size- and pH-Dependent Catalytic Activity of Gold Nanoparticles

Using UV–vis spectrophotometry to track the absorbance decay of H_2O_2 at λ = 240 nm (the molar extinction coefficient of H_2O_2: ϵ_{240} = 39.4 M^{-1}cm^{-1}), the catalytic properties of individual AuNPs of 3 and 30 nm were studied. **Figure 1** shows the kinetic curves of H_2O_2 self-decomposition and its decomposition under the influence of nanoparticles of two sizes. For these measurements, pH = 7.4 of the reaction was chosen as the closest to physiological conditions. The self-decomposition of hydrogen peroxide at this pH is quite negligible, while rapid acceleration of this process is observed when gold nanoparticles are introduced to the system. As expected, the smaller size of the catalyst has led to a more significant increase in velocity compared to 30 nm particles. This effect is associated with a higher number of active sites on the surface available for catalysis in the case of smaller nanoparticles due to the larger surface area for the same mass of substance. For further comparison of catalytic effects, the reaction rate of H_2O_2 decomposition was calculated as a negative slope in the linear range of the kinetic curves of 'concentration versus time'. For consistency, the reaction rate during the first 5 h was used for all samples described from now on. Most catalase-mimicking nanomaterials typically increase their catalase-like activity under basic conditions rather than at physiological pH and especially under acidic conditions.[20] Its driving force is considered to be the pre-adsorption of OH groups on the surface of the catalyst, which are only favorable under basic conditions.[23] To explore whether this mechanism applies to our system, we measured catalase-like activity at different pH levels, and Figure 1b shows the effect of pH on the oxygen formation rate. Regardless of the surface area exposed to catalysis, catalase-like activity increases with an increase in pH. For further experiments, two pH values were chosen: 7.4 to mimic physiological conditions and 7.0 as the closest to the environment of the cancer cell.[44]

2.2. Quality Assessment of Catalytic Activity of AuNPs

2.2.1. Mass Spectrometry

Mass spectrometry detection of catalytic oxygen results (**Figure 2a**) of two solutions of 3 nm 10 μgml^{-1} AuNPs, at pH 7 and 7.4 indicate a drastic increase in oxygen gas pressure after addition of 100mM H_2O_2 to the system. It indicates that it is indeed molecular oxygen (O_2), which is a product of hydrogen peroxide decomposition.

2.2.2. EPR

A spin-trapping electron paramagnetic resonance (EPR) technique has been used to demonstrate the production of oxygen by AuNPs. Molecular oxygen (O_2) is paramagnetic,

© 2024 Wiley-VCH GmbH

15214117, 2024, 5, Downloaded from https://onlinelibrary.wiley.com/doi/10.1002/ppsc.202300149 by ITMO University, Wiley Online Library on [17/07/2024]. See the Terms and Conditions (https://onlinelibrary.wiley.com/terms-and-conditions) on Wiley Online Library for rules of use; OA articles are governed by the applicable Creative Commons License

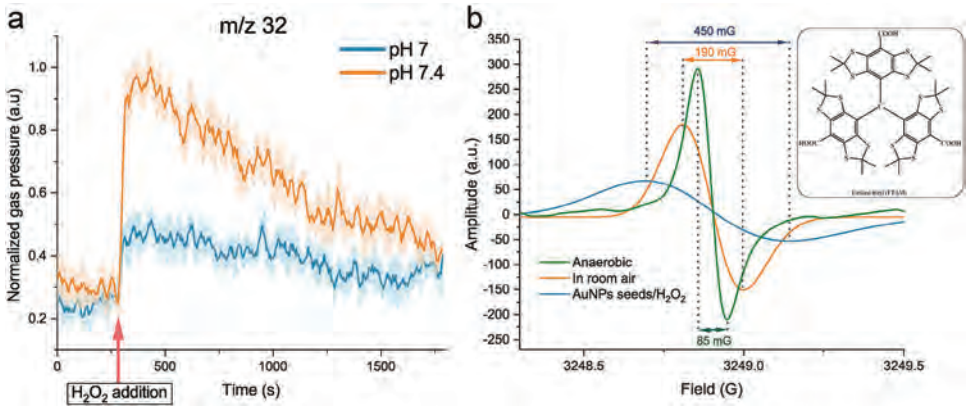

Figure 2. a) Mass-spectrometry measurements of oxygen, red arrow represents the time in which 100 mM H_2O_2 was added to the 10 μgml^{-1} AuNPs mixture. Blue line – at pH 7, orange – at pH 7.4; b) EPR spectra of 50 μM FTAM in 0.1 M phosphate buffer pH = 7.4 in anaerobic conditions (green), in air (orange), and after incubation with 10 μgml^{-1} AuNPs and 100 mM H_2O_2 (blue). The inset represents the FTAM molecular structure.

therefore bimolecular collision with trityl radicals as spin probe results in Heisenberg spin exchange interaction and subsequent broadening of the observed EPR signal. This phenomenon is used for oxygen detection.[45] Trityl radicals are also known as promising contrast agents for in vivo oximetry and tissue oxygen mapping.[46,47] Typically, they demonstrate a single, narrow EPR signal (linewidth < 100 mG), without hyperfine couplings, unlike nitroxide radicals with significantly broader multiplet signal (linewidth ca. 1000 mG), which are commonly used for the investigation of AuNP catalase activity.[22] In addition, trityl radicals show high selectivity for detecting oxygen in the presence of superoxide and other reactive oxygen species (ROS).[48] FTAM (Figure 2b, inset) was chosen for EPR spectroscopic oxygen measurements due to its availability and well solubility in water, since three carboxylic groups of this radical exist in the ionized form at biological pH (pH 7.4).[49]

The EPR spectra recorded at room temperature (23 °C) in phosphate buffer solutions (0.1 M, pH = 7.4) saturated with argon, in air and for AuNP seeds after 100 mM hydrogen peroxide addition are shown in Figure 2b. The solution of 50 μM FTAM was separated from the nanoparticles by a gas-permeable membrane during the catalase reaction. In the absence of molecular oxygen, the EPR signal consists of a single sharp peak with a peak-to-peak line width of 100 mG, line broadening appeared in room air and reached its maxima with line width of 190 mG, which corresponds to ca. 20% of oxygen and in good agreement with the percent oxygen in air.[45] The significant broadening of the EPR signal was observed for the dispersion containing the AuNPs seeds, the peak-to-peak line width became 450 mG attributed to ca. 85% of oxygen.[49] These results demonstrate that ultra-small gold nanoparticles are capable of generating considerable amounts of molecular oxygen using hydrogen peroxide as a source.

2.3. Capsules Size and Concentration

Capsules were synthesized according to the materials section (Capsule preparation) and **Figure 3**. The zeta potential of each layer was determined by the Zetasizer Nano ZS (**Figure 4a**). The size of the capsules was determined using NTA and Cryo-TEM measurements (Figure 4b–g). Their concentrations were determined using NTA measurements, AuNPs and PS were found using ICP-MS findings (Table S1, Supporting Information). The amount of gold NPs per capsule was calculated using the formula: $N = \frac{V'}{V} = \frac{m/\rho}{4/3\pi R^3}$, where V' is the volume of gold taken, V is the volume of one gold nanoparticle, m is a mass of gold taken, $\rho = 19.3$ gcm^{-3} is a density of gold, and R is the radius of NPs. The AuNPs radius (R) was considered to be 1.5 nm on the basis of Cryo-TEM measurements. The maximum concentration of PS for the experiment was set at 2 μgmL^{-1} and the maximum AuNPs concentration was calculated based on this value (Table S1, Supporting Information). Judging from the size distribution of Cryo-TEM images (Figure 4b–g, insets), it was confirmed that the approximate sizes of the capsules were, indeed, 300 and 700 nm. The capsules maintain a rounded, slightly elliptical shape.

2.4. Capsules Aqueous Suspension Spectral Characteristics

To evaluate capsules suspension spectral characteristics their extinction, photoluminescence (PL), and photoluminescence excitation (PLE) measurements were performed. Figure 4h shows the extinction spectra of colloidal solutions of capsules loaded with AuNPs, PS and their mixture, as well as the absorption spectrum of empty capsules and extinction spectra of aqueous solutions of PS and AuNPs. A number of characteristic bands corresponding in shape and position (676 and 350 nm) to the monomeric form of aluminum phthalocyanine are observed in the extinction spectrum of an aqueous solution of PS. In the extinction spectra of capsules with PS and PS+AuNPs, the position of the long-wavelength extinction band aluminum phthalocyanine corresponding to the electronic transition $S_0 \rightarrow S_1$ is shifted to the region of lower energies, and the band itself undergoes a noticeable broadening. The observed change in the position and shape of the absorption band of aluminum phthalocyanine indicates the formation of aggregates on the surface of the shell of the capsules as a result of partial charge loss during the electrostatic interaction of phthalocyanine molecules with positively

© 2024 Wiley-VCH GmbH

15214117, 2024, 5, Downloaded from https://onlinelibrary.wiley.com/doi/10.1002/ppsc.202300149 by ITMO University, Wiley Online Library on [17/07/2024]. See the Terms and Conditions (https://onlinelibrary.wiley.com/terms-and-conditions) on Wiley Online Library for rules of use; OA articles are governed by the applicable Creative Commons License

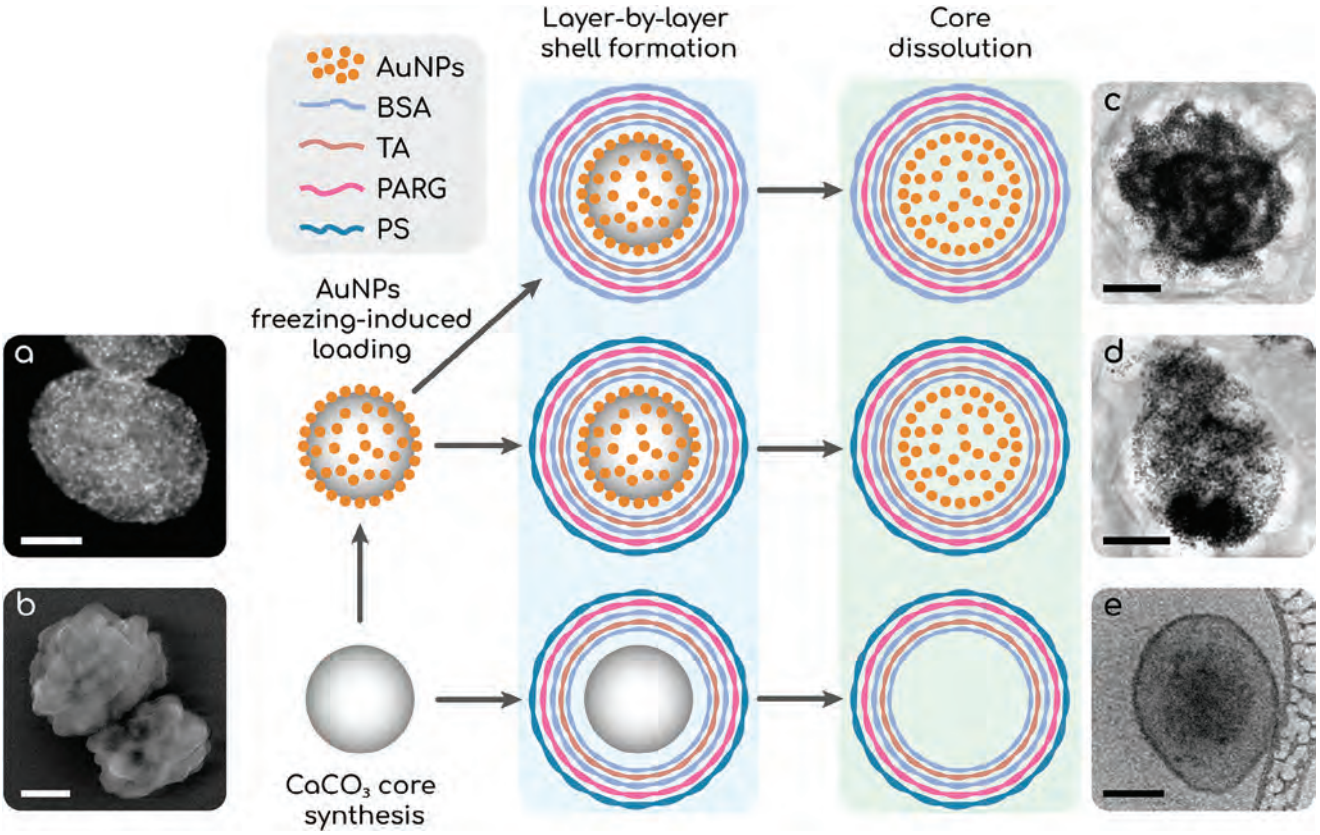

Figure 3. Capsules synthesis scheme. a) $CaCO_3$ particles after AuNPs loading SEM image; b) $CaCO_3$ particles SEM image; c) capsules with AuNPs Cryo-TEM image; d) capsules with AuNPs and PS Cryo-TEM image; e) capsules with PS Cryo-TEM image. Scale bar – 100 nm.

charged groups of the polymer shell. This behavior of tetrapyrrole compounds is well known and has been well studied. In particular, work by Palewska et al.[50] showed that metal complexes of phthalocyanines form aggregates as a result of π stacking, and Martynenko et al.[51] presented a model describing the patterns of aggregation of aluminum phthalocyanine (Photosens) as a result of the electrostatic interaction of molecules with charged groups of molecules of stabilizers of the surface of CdSe/ZnS quantum dots. Figure 4i shows the luminescence spectra of an aqueous solution of PS and a sample with capsules loaded with PS and AuNPs, as well as their luminescence excitation spectrum. The analysis of the data shown in Figure 4i showed that the luminescence spectra of an aqueous solution of the monomeric form of PS and luminescence of a sample with capsules practically coincide with each other, and the luminescence excitation spectrum of a sample with capsules contains bands whose position corresponds to the extinction spectrum of the aluminum phthalocyanine monomer and differs from the extinction spectrum of capsules with PS (Figure 4h). The data obtained are in good agreement with the ideas about the photophysical properties of phthalocyanine aggregates.

2.5. XPS Measurements

The Au4f spectrum of initial AuNPs was modeled with a single doublet with the binding energy (BE) of $Au4f_{7/2}$ line of 84.1 eV, which corresponds to the metallic state.[52] The Au4f spectrum of capsules with AuNPs and PS+AuNPs could be deconvoluted into two doublets. The first doublet (Au(0)) with BE($Au4f_{7/2}$) = 84.1 eV corresponds to the metallic state of the core of gold nanoclusters. The second doublet (Au(I)) with BE = 85.5 eV for capsules with AuNPs and with BE = 84.8 eV for capsules with PS+AuNPs corresponds to the states linked to BSA of the shell of nanoclusters.[53] The relative concentrations of Au(I) states for capsules with AuNPs and capsules with PS+AuNPs are 80% and 75%, respectively. The resulted graph are shows at Figure S1, (Supporting Information).

2.6. Capsules Degradation and PS Release

To evaluate a degradation time of capsules, two solutions were used. The first is a human plasma isolated from blood by precipitation, and the second is a solution that simulates the conditions of the intestinal environment. To prepare the second mixture, 2.0 mL of 18 $mgmL^{-1}$ pancreatin and 2.0 mL of 120 mM bile salts were added to 10 ml of 0.1 M $NaHCO_3$ solution (pH 7) (final pancreatin concentration was 12 USP/mg). Capsules in PBS solution were used as control samples. The mixtures were kept at 37 °C on the thermostat. The release process was evaluated by measuring PS absorption at 672 nm in the supernatant after sedimentation of the capsules at specified points in time. The results (Figure S2, Supporting Information) indicate that after 24 h around 90% of

© 2024 Wiley-VCH GmbH

15214117, 2024, 5, Downloaded from https://onlinelibrary.wiley.com/doi/10.1002/ppsc.202300149 by ITMO University, Wiley Online Library on [17/07/2024]. See the Terms and Conditions (https://onlinelibrary.wiley.com/terms-and-conditions) on Wiley Online Library for rules of use; OA articles are governed by the applicable Creative Commons License

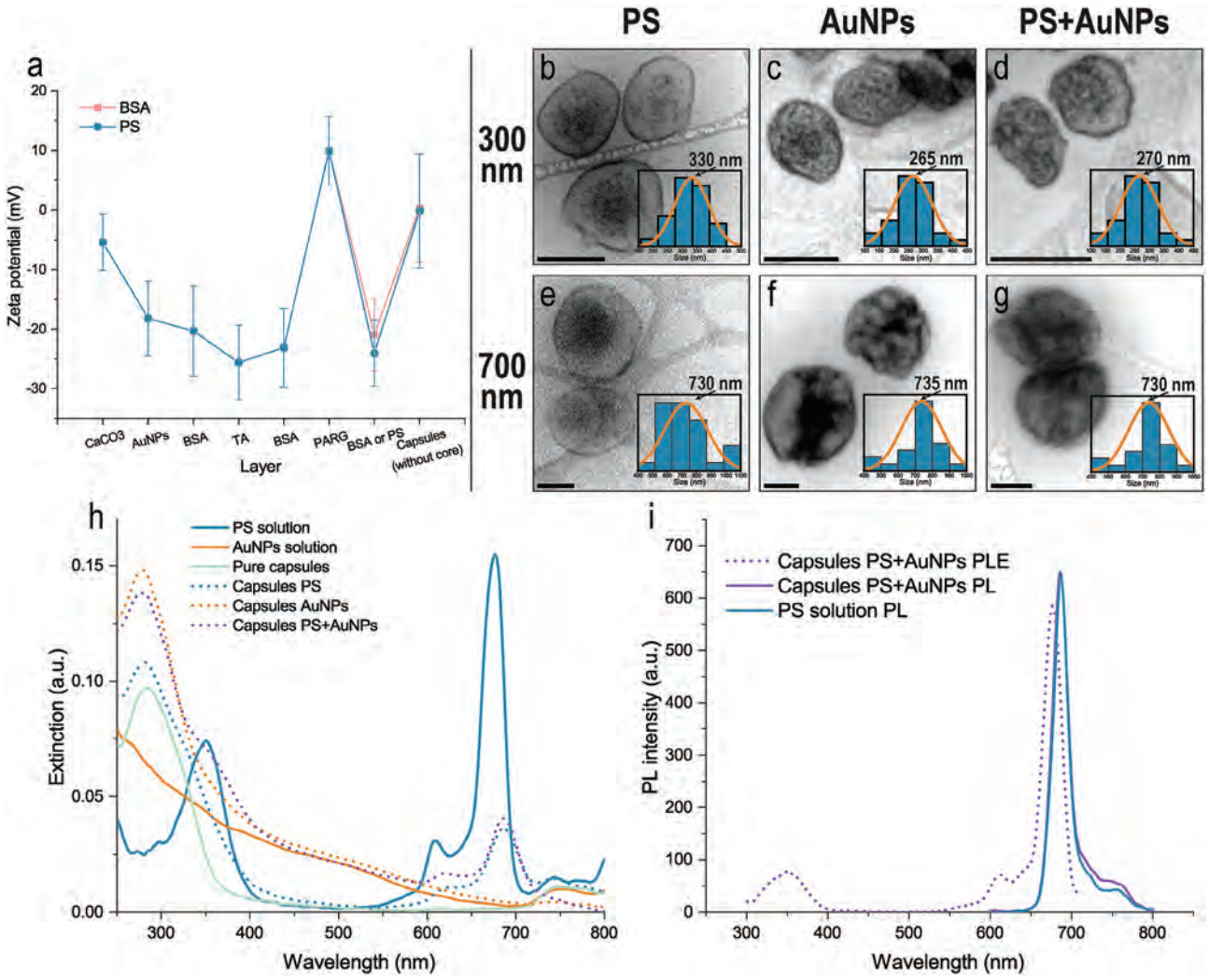

Figure 4. a) Zeta-potential measurements. Error bars represent the SD (n = 3); b–g) Cryo-TEM images of capsules, inset represents size distribution measurements from Cryo-TEM images. 300 and 700 nm – capsules with approximate diameter of 300 and 700 nm, respectively. PS – capsules with photosensitizer only, AuNPs – capsules with gold nanoparticles only; PS+AuNPs – capsules with photosensitizer and AuNPs. Scale bar – 250 nm; h) Extinction measurements. Here, blue line represents PS solution measurement, brown - AuNPs solution, green - pure capsules, blue dot line - capsules with PS, brown dot line - capsules with AuNPs and purple dot line - capsules with PS and AuNPs; i) Photoluminescence (PL) and photoluminescence excitation (PLE) measurements. Here, purple dot line represents the PLE spectra of capsules with PS and AuNPs, purle line - PL spectra of capsules with PS and AuNPs and blue - PL spectra of the PS solution.

the encapsulated PS had already been released. The absorbance of the mixtures in PBS was not different at 672 nm, and therefore the capsules showed no degradation.

2.7. Catalytic Activity of Capsules with AuNPs

The catalase-like activity of individual seeds was compared with the seeds loaded into polymeric capsules of two sizes: 300 and 700 nm, to determine the dependency of the capsules size on the reaction. For quantitative comparison, each experiment was normalized on gold concentration equal to 0.3 mgmL^{-1} based on ICP-MS findings. As shown in **Figures** 5a,b, the decomposition of H_2O_2 in three different systems has common decay characteristics over time for individual and encapsulated AuNPs. However, a drastic decrease in the reaction rate is observed for gold-containing capsules (Figure 5c). However, counter-intuitively, the reaction velocity did not drop to zero in these cases. This effect might be attributed to the permeability of capsules' polymeric shells to small molecules as H_2O_2, as it was described before.[54] Capsules with this characteristic of permeability, in our opinion, could be used successfully as microreactors with controlled consumption of H_2O_2 and release of oxygen.

2.8. AuNPs Stability

The stability of gold nanoparticles was investigated under different conditions: initial gold nanoparticles and gold nanoparticles encapsulated in polymeric capsules, gold nanoparticles after a

© 2024 Wiley-VCH GmbH

15214117, 2024, 5, Downloaded from https://onlinelibrary.wiley.com/doi/10.1002/ppsc.202300149 by ITMO University, Wiley Online Library on [17/07/2024]. See the Terms and Conditions (https://onlinelibrary.wiley.com/terms-and-conditions) on Wiley Online Library for rules of use; OA articles are governed by the applicable Creative Commons License

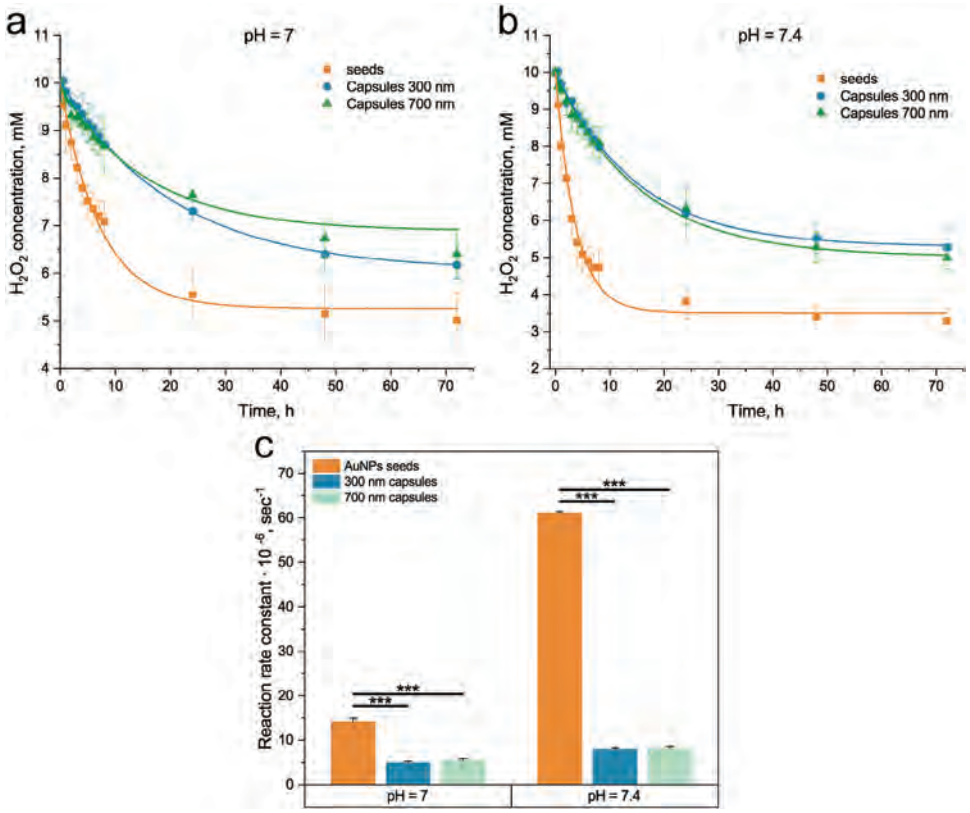

Figure 5. Kinetic curves of H_2O_2 decomposition a) at pH = 7, b) at pH = 7.4. Error bars represent the SD (n = 3); c) Reaction rate constant dependence on pH and catalyst type. All samples were normalized to gold concentration, 10 $\mu g ml^{-1}$. Error bars represent the SD (n = 3). A statistically significant difference is indicated by *** at $P < 0.0001$, obtained using a two-level ANOVA.

catalytic reaction, and of gold nanoparticles within capsules after the reaction, and finally, the stability of both samples of gold nanoparticles was evaluated over a period of 6 months at 4 °C (**Figure 6**). The results indicated that the initial gold nanoparticles are relatively stable in solution after 6 months, but are more susceptible to growth (Figure 6c), due to Ostwald ripening.[55] The encapsulation of gold nanoparticles prevents the stabilizer from being washed out and therefore prevents its growth (Figure 6f). The catalytic reaction also promotes the aggregation of nanoparticles due to the formation of passivating layers on their surface and oxidation of the stabilizer[56] (Figure 6a). On the other hand, the use of encapsulated gold nanoparticles prevents it from occurring (Figure 6d,g). As a result, AuNPs encapsulation prevents their growth over time and after the catalytic reaction (Figure 6g).

2.9. Cell Viability

To estimate cell viability for pure photosensitizer, solutions with different concentrations were applied to SKOV-3 and CHO cells and irradiated with LD = 20 $J cm^{-2}$. 96-well plate was divided into dark and light-irradiated half, to provide all necessary controls. The toxicity results are shown in **Figure** 7a,d and IC_{50} calculations for both cell lines are shown in **Figure** 8 and Table S2, Supporting Information. IC_{50} values for pure PS are comparable to the data presented by Sololova et al.[57].

2.10. Cell Viability for Capsules

To estimate cell viability after capsules irradiation – different types of capsules were placed in a 96-well plate with concentration changing based on PS concentration mass compound: 2000, 1000, 500, 250, and 125 $ng mL^{-1}$ (Figure S3, Supporting Information). AuNPs concentrations were changing accordingly: 20, 10, 5, 2.5 and 1.25 $\mu g mL^{-1}$. Two plates for each type of cells were prepared to check the dark and light toxicity of the compounds. One of them was irradiated with LD = 20 $J cm^{-2}$ (see protocol details in the Materials section, Cell experiment). To calculate cell viability, wells without any treatment, light and capsules, were used as control wells, and the number of cells in the experimental wells were divided by them. Examples of images analyzed in control wells and under the influence of capsules with AuNPs are shown in Figure S4, Supporting Information; and after cell irradiation, incubated with capsules, containing PS and AuNPs in **Figure 9**. The results of cell viability measurements for dark toxicity (Figure S5, Supporting Information) and light irradiation (Figure 7b,c,e,f) as well as IC_{50} calculations (Figure 8; Table S2, Supporting Information) show a good dependence (≈2 times) on the presence of AuNPs with PS inside one capsule compared to capsules containing only PS or AuNPs for both sizes, 300 and 700 nm, and both cell lines, SKOV-3 and CHO. Although the IC_{50} for CHO cells is lower than one for SKOV-3, it showed no significant difference between PS and PS+AuNPs capsules.

© 2024 Wiley-VCH GmbH

15214117, 2024, 5, Downloaded from https://onlinelibrary.wiley.com/doi/10.1002/ppsc.202300149 by ITMO University, Wiley Online Library on [17/07/2024]. See the Terms and Conditions (https://onlinelibrary.wiley.com/terms-and-conditions) on Wiley Online Library for rules of use; OA articles are governed by the applicable Creative Commons License

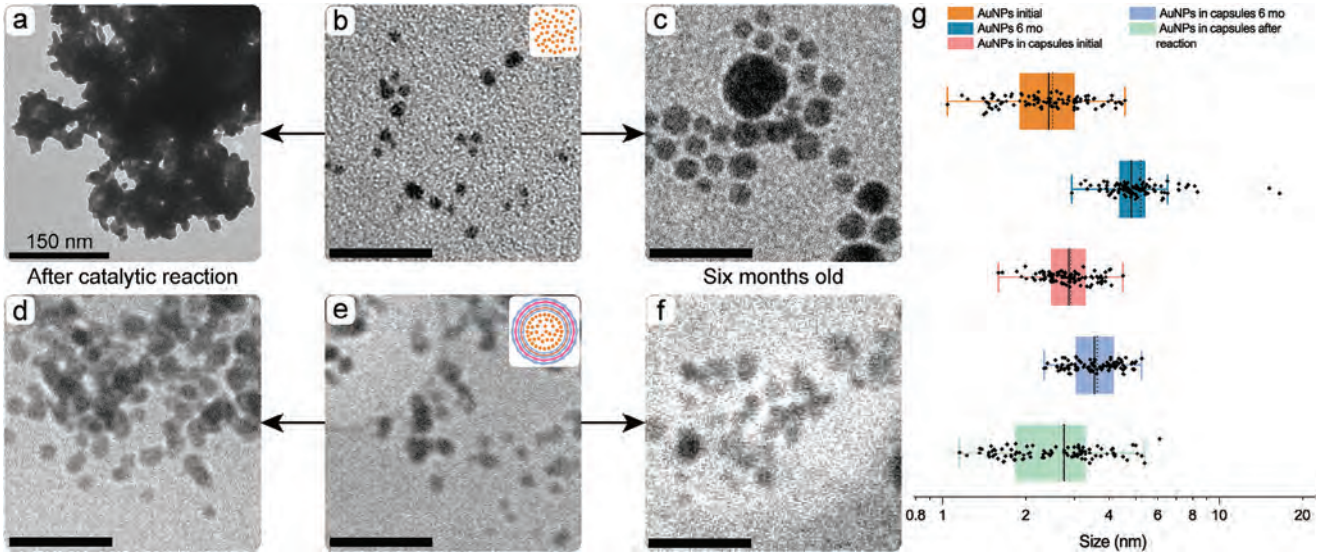

Figure 6. AuNPs stability measurements. Cryo-TEM images: a) AuNPs after catalytic reaction, b) Initial AuNPs, inset represents schematic illustration of the sample, c) AuNPs after 6 months at 4°C, d) AuNPs in capsules after catalytic reaction, e) Initial AuNPs in capsules, inset represents schematic illustration of the sample, f) AuNPs in capsules after 6 months at 4°C. In all images except for (a) scale bar - 20 nm. g) Size distribution from TEM images of initial AuNPs, AuNPs after 6 months at 4°C, initial AuNPs in capsules, AuNPs in capsules after 6 months at 4°C and AuNPs in capsules after catalytic reaction. The solid line represents the median value, dot line - mean, the box borders represent SD and error bars - 95% confidence interval. Number of measured nanoparticles - 100.

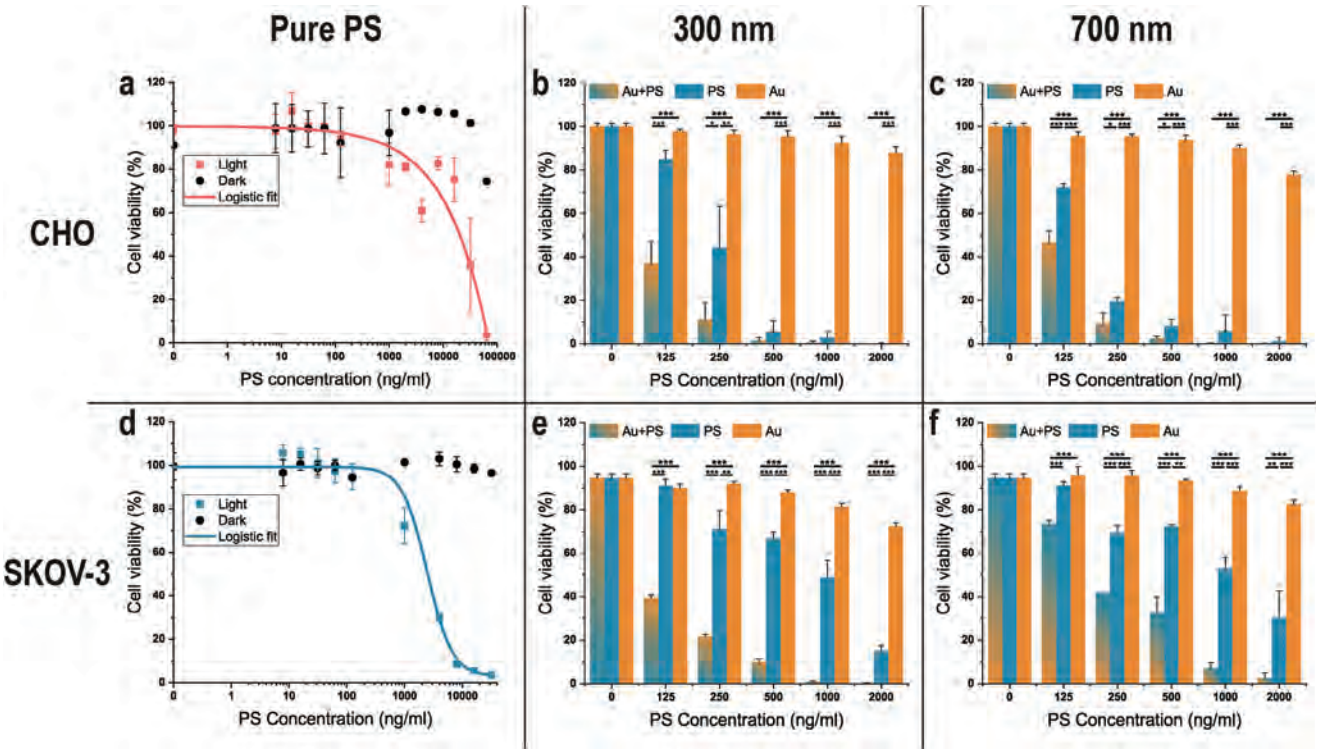

Figure 7. Cell viability measurements for Pure PS a) CHO cell line, d) SKOV-3 cell line, lines represent logistic fit. Error bars represent the SD (n = 3); Cell viability measurements for capsules: b) 300 nm capsules, CHO cell line; c) 700 nm capsules, CHO cell line; e) 300 nm capsules, SKOV-3 cell line; f) 700 nm capsules, SKOV-3 cell line. The orange bar represents capsules containing gold nanoparticles only, blue – only photosensitizer, blue-orange – both, photosensitizer and gold nanoparticles. Error bars represent the SD (n = 3). A statistically significant difference is indicated by * at $P < 0.01$, ** at $P < 0.001$ and *** at $P < 0.0001$, obtained using a two-level ANOVA.

© 2024 Wiley-VCH GmbH

15214117, 2024, 5, Downloaded from https://onlinelibrary.wiley.com/doi/10.1002/ppsc.202300149 by ITMO University, Wiley Online Library on [17/07/2024]. See the Terms and Conditions (https://onlinelibrary.wiley.com/terms-and-conditions) on Wiley Online Library for rules of use; OA articles are governed by the applicable Creative Commons License

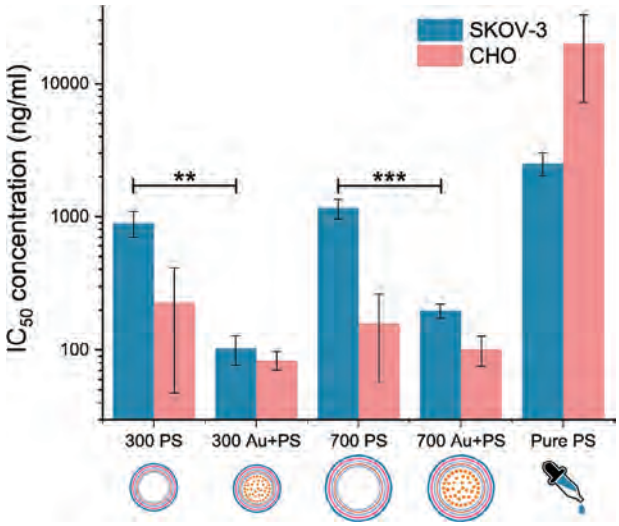

Figure 8. IC_{50} calculations. The blue bar represents SKOV-3 cell line, red – CHO cell line. Error bars represent the SD (n = 3). A statistically significant difference is indicated by * at $P < 0.01$, ** at $P < 0.001$ and *** at $P < 0.0001$, obtained using a two-level ANOVA.

3. Conclusion

In summary, we fabricated light-responsive catalase-like microreactors based on gold nanoparticles and photosensitizer molecules incorporated into polymeric capsules following the LbL approach for simultaneous ROS generation and oxygen production. Encapsulation of AuNPs prevents their growth in time and after catalytic reaction. Polymeric submicrocapsules loaded with gold nanoparticles by the FIL method present a high catalytic activity in the hydrogen peroxide decomposition reaction, which results in in situ formation of molecular oxygen. This reaction follows the first-order kinetics with reaction rate constant $k =$ 5.2 and 8.1 s^{-1} for pH 7 and 7.4, respectively, which is comparable to the value obtained for tetrakis(hydroxymethyl)phosphonium chloride stabilized gold nanoparticles (k = 14.2 and 61.1 s^{-1} for pH 7 and 7.4, respectively). After 24 h in human plasma, the developed polymer capsules almost completely degraded, with a release of about 90% of gold nanoparticles. Thus, the structural integrity of a capsule is preserved for a prolonged period of time, preventing aggregation of the encapsulated entity and allowing the capsule to function as a durable biocatalytic microreactor. According to our validation TME cell model, the polymeric submicrocapsules exhibit remarkable light-induced cytotoxicity in comparison to individual photosensitizers or gold nanoparticles, suggesting a synergistic effect between photodynamic action and catalase reaction. The IC_{50} for the SKOV-3 cell line is 100±26 and 890±197 $ngmL^{-1}$ for capsules with AuNP + PS and PS only, respectively, while the IC_{50} for pure photosensitizer is 2515±490 $ngmL^{-1}$. This potentially makes them suitable for PDT against tumor hypoxia.

4. Experimental Section

Materials: Bovine serum albumin (BSA), tannic acid (TA), phosphate-buffered saline (PBS), chloroauric acid ($HAuCl_4$), trisodium citrate

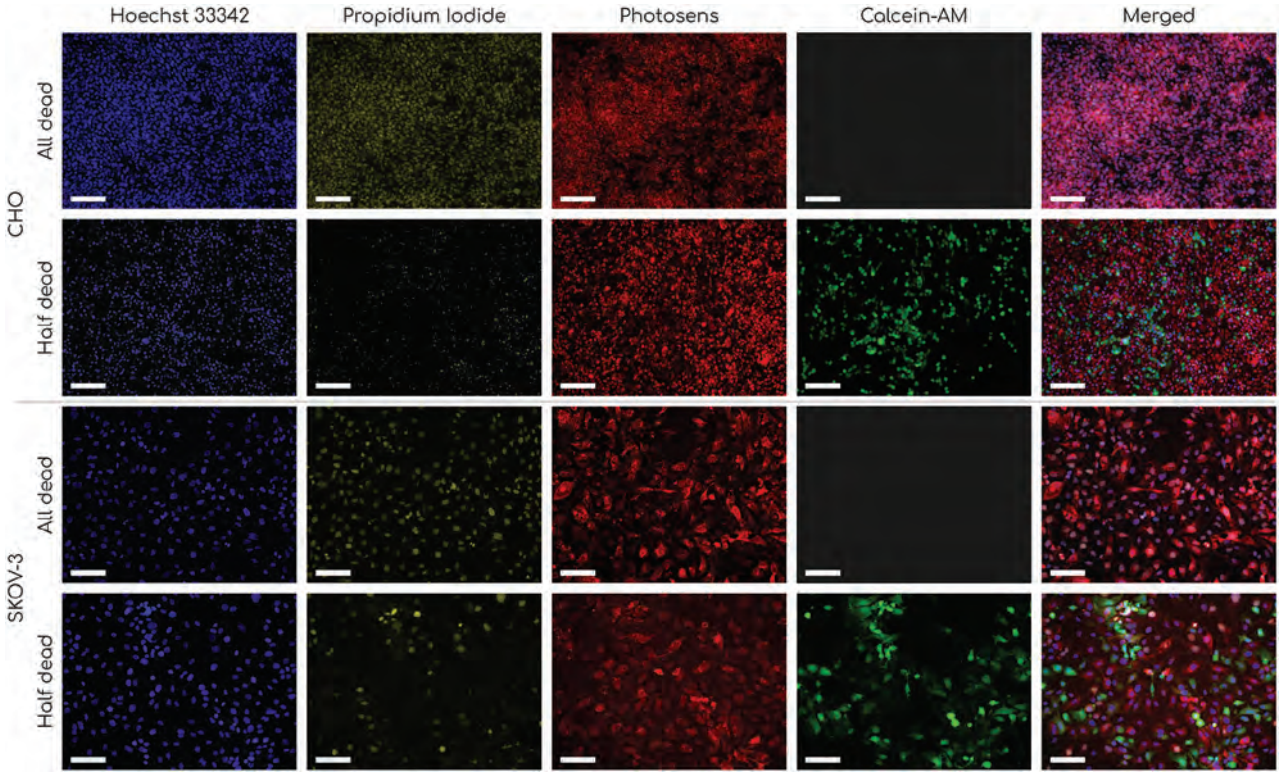

Figure 9. Fluorescent microscopy images of CHO and SKOV-3 cells after incubation with capsules, containing gold nanoparticles and photosensitizer and after irradiation with all cells dead and IC_{50} concentrations. Blue – Hoechst 33342, green – Calcein-AM, yellow – propidium iodide, red – photosensitizer. Scale bar - 100 μm.

© 2024 Wiley-VCH GmbH

15214117, 2024, 5, Downloaded from https://onlinelibrary.wiley.com/doi/10.1002/ppsc.202300149 by ITMO University, Wiley Online Library on [17/07/2024]. See the Terms and Conditions (https://onlinelibrary.wiley.com/terms-and-conditions) on Wiley Online Library for rules of use; OA articles are governed by the applicable Creative Commons License

($Na_3C_6H_5O_7$), Poly-L-arginine hydrochloride, hydrochloric acid, sodium chloride, calcium chloride dehydrate, anhydrous sodium carbonate, glycerol and ethylene glycol (EG) were purchased from Sigma—Aldrich (St. Louis, Missouri, USA). RPMI 1640 Medium, fetal bovine serum (FBS), DPBS, penicillin & streptomycin and trypsin-EDTA were purchased from GIBCO (Barcelona, Spain). Calcein AM, propidium iodide (PI), and Hoechst 33342 dyes were purchased from Invitrogen Corporation (Waltham, Massachusetts, USA). Photodynamic dye (PS), Photosens (a mixture of di-, tri- and tetraaluminum phthalocyanine) was purchased from Federal State Unitary Enterprise "State Scientific Centre NIOPIK" (Russia), its spectrum is shown on Figure S6c, (Supporting Information). Finland trityl radical (FTAM) was a commercial sample provided kindly by the Metal Complex Catalysis Groups of the N.N.Vorozhtsov Novosibirsk Institute of Organic Chemistry SB RAS (Russia). All chemicals were used without further purification. Deionized (DI) water (18.2 MΩ ·cm) from a Milli-Q Plus 185 Water Purifier, Millipore (Burlington, Massachusetts, USA) was used to make all solutions.

Samples Preparatiom: *Synthesis of Gold Nanoparticles 3 nm Seeds*: A protocol reported by Duff et al.[58] was used to synthesize AuNPs: 9.25 mL of water was added to 0.5 mL of 1 M NaOH and 12µL of tetrakis (hydroxymethyl) phosphonium chloride. To the stirred solution, 0.5 mL of 8% $HAuCl_4$ was quickly added. A dark brown color was observed in the reaction mixture, which indicated that gold nanoparticles with a size around 3 nm had formed.[59]

Synthesis of Gold Nanoparticles 30 nm: A solution of 75 mg of hydrochloric acid in distilled water was placed in a round-bottom flask equipped with a reflux condenser, and the temperature was slowly increased with a thorough stirring, in order to bring the solution to a boil. The solution was continued to boil for an hour, with 20 ml of 1% warm sodium citrate solution added. The solution was then cooled to room temperature with thorough stirrings. Further particles were used in the form of a stable colloid solution. Size of the gold nanoparticles, according to transmission electron microscopy, 30±6 nm, Z-potential -30±5 mV.

$CaCO_3$ Particle Synthesis: Submicron $CaCO_3$ vaterite cores with a size ≈600–800 nm were synthesized according to Trushina et al.[60] Briefly, 400 µL of 0.5 M $CaCl_2$ and 0.5 M Na_2CO_3 solutions were added to 4 g of glycerol in a glass vial on a magnetic stirrer at a speed of 700 rpm and a temperature of 30 °C. The stirring was stopped after one hour, the suspension of particles was centrifuged at 13000 rpm for 5 min and washed twice with DI water at 9000 rpm for 1 min. The particles were then dried at 60 °C for later use.

$CaCO_3$ vaterite cores of size ≈200–300 nm were synthesized according to Bahrom et al.[61] Briefly, 10 ml of solutions of 4.9 mM $CaCl_2$ and 25 mM $NaHCO_3$ in EG (water: EG ratio = 3:20) were mixed under magnetic stirring at 700 rpm. The stirring was stopped after 30 min, the suspension of particles was centrifuged at 13000 rpm for 5 min and washed twice with ethanol at 13000 rpm for 1 min. The particles were then dried at 60 °C for later use.

Loading with AuNPs: The loading of $CaCO_3$ cores was performed with the freezing-induced loading (FIL) technique[62] using the TetraQuant R-1 mini-rotator (TetraQuant LLC, Russian Federation). Briefly, 1 mL of AuNPs suspension was added to the calcium carbonate cores in the US bath. The obtained suspension was frozen under constant rotation at -20 °C for 1 h. Subsequently, the samples were washed three times with DI water, and the FIL sequence was repeated six times to obtain the maximum possible load. The AuNPs concentration in the mixture was calculated afterward with the ICP-MS method.

Capsules Preparation: Synthesized $CaCO_3$ particles were used as a core for creating polymeric submicrocapsules. Capsules were obtained by adsorption of BSA (2 $mgmL^{-1}$), TA (2 $mgmL^{-1}$), PARG (1 $mgmL^{-1}$) and PS (1 $mgmL^{-1}$) on the surface of the vaterite particles using the Layer-by-Layer method. Thus, the capsule shell consisted of five layers: BSA/TA/BSA/PARG/BSA or BSA/TA/BSA/PARG/PS. (Figure 3). Subsequently, the vaterite cores were dissolved with HCl solution (0.1 M), resulting in the formation of polymer capsules. After each stage of adsorption, as well as after dissolution of the vaterite cores, the capsule suspension was purified by centrifugation (2 min, 13000 rpm) and washed twice with 1 ml of DI water.

Characterization: *Dynamic Light Scattering (DLS) and Zeta-Potential Measurements*: Size and zeta-potential measurements were performed on the ZetaSizer Nano ZS analyzer (Malvern Panalytical, Malvern, UK). For zeta-potential measurements, all samples were diluted approximately 20 times in DI water and placed in a U-shaped cuvette; for size measurements, all samples were diluted 40 times in DI water and placed in the plastic cuvette. The results were processed by ZetaSizer Software 8.00. Each measurement was carried out at 25 °C and repeated three times.

Extinction Spectra Measurements: Extinction spectra measurements of nanoparticles, core-shell structures, and capsules were performed with a Tecan Infinite M Nano + multifunctional microplate reader (Tecan Trading AG, Männedorf, Switzerland) and UV-Probe 3600 spectrophotometer (Shimadzu, Japan) at room temperature (25 °C).

Photoluminescence and Photoluminescence Excitation Spectra Measurements: The steady-state PL and PLE spectra were obtained with Cary Eclipse spectrofluorometer (Agilent, Santa Clara, CA, USA).

Scanning Electron Microscopy with Energy-Dispersive X-Ray Spectroscopy (SEM EDX): Surface morphology and the elemental composition of the particles were characterized by a scanning electron-microscope (SEM) MAIA3 (Tescan, Brno, Czech Republic) coupled with an energy dispersive X-ray spectroscope (EDS) X-act (Oxford Instruments, Abingdon, UK). Particle solution in water was dropped on a silicon wafer and dried under ambient conditions. Particle images were obtained at a 15 kV accelerating voltage in the secondary electron (SE) and back-scattered electron (BSE) detection modes.

Inductively Coupled Plasma Mass Spectrometry (ICP-MS): The concentrations of elements in particles were quantified by inductively coupled plasma mass-spectrometry using a NexION 2000 spectrometer (Perkin Elmer, Waltham, MA, USA). The particles were dissolved in concentrated aqua regia, a 3:1 mixture of HCl:HNO_3, and diluted with water to the acid concentration 30% for the measurements. ^{31}P, ^{43}Ca and ^{79}Au peaks were used for the analysis.

EPR: EPR measurements were performed at room temperature (23 °C). A Varian E-4 X-band spectrometer operating at ≈9.2 GHz was used. This spectrometer had been upgraded to connect to a personal computer. Liquid samples with a typical volume of 30 µL were placed in open glass capillary tubes. EPR signals as the first derivative of the microwave absorption were collected at sub-saturating microwave power 1 mW using 100 kHz modulation of 0.1 Oe peak-to-peak amplitude with a typical spectrum scanning time of 2 min.

Finland trityl radical (FTAM) was used for molecular oxygen detection. To separate the oxygen generator substance from FTAM, two 0.6 mL eppendorf tubes were soldered to each other by caps with a hole drilled in the middle. Between these tubes, a piece of 500 Da dialysis bag was placed. Placing the eppendorfs vertically on each other, locating the reaction media on the lower tube, and FTAM on the upper tube allowed gas transfer through the dialysis membrane, preventing the transfer of large molecules.

Mass Spectrometry Detection of Catalytic Oxygen Release: To estimate the catalytic reduction of hydrogen peroxide on the surface of the gold nanoparticle, mass spectrometry detection of released oxygen was implemented. On the basis of this, a mass spectrometer with a direct inlet and a quadrupole mass analyzer Universal Gas Analyzer UGA-100 (SRS, USA) was used. 2 mL suspension of gold nanoparticles (C = 0.2 mgL^{-1}) in the phosphate buffer of chosen pH (7 or 7.4) was placed in a 10 mL flask sealed with a rubber septum, where 1 mL of hydrogen peroxide was added using a micro syringe after 5 min of measurements. During the catalytic reduction of hydrogen peroxide, a constant argon flow of 100 $mLmin^{-1}$ was pumped through the suspension volume, which helps to transfer the released oxygen molecules into the ionization source chamber (Electron energy 70 eV) of the mass spectrometer. In addition, control samples without H_2O_2 or gold nanoparticles were also measured.

Cryo-TEM: A copper grid (200 mesh) with lacey carbon cover was made hydrophilic by air plasma treatment. 3 µL of the sample was placed on the hydrophilic grid under 100% humidity conditions. The excess of the sample was removed by blotting the grid for 1 s with filter paper. Then, the grid was plunged into liquid ethane (automated plunging system, Vitrobot FEI, USA). The prepared grid was transferred in liquid nitrogen to cryo-TEM (Transmission electron microscope Tecnai G212 SPIRIT, FEI,

© 2024 Wiley-VCH GmbH

15214117, 2024, 5, Downloaded from https://onlinelibrary.wiley.com/doi/10.1002/ppsc.202300149 by ITMO University, Wiley Online Library on [17/07/2024]. See the Terms and Conditions (https://onlinelibrary.wiley.com/terms-and-conditions) on Wiley Online Library for rules of use; OA articles are governed by the applicable Creative Commons License

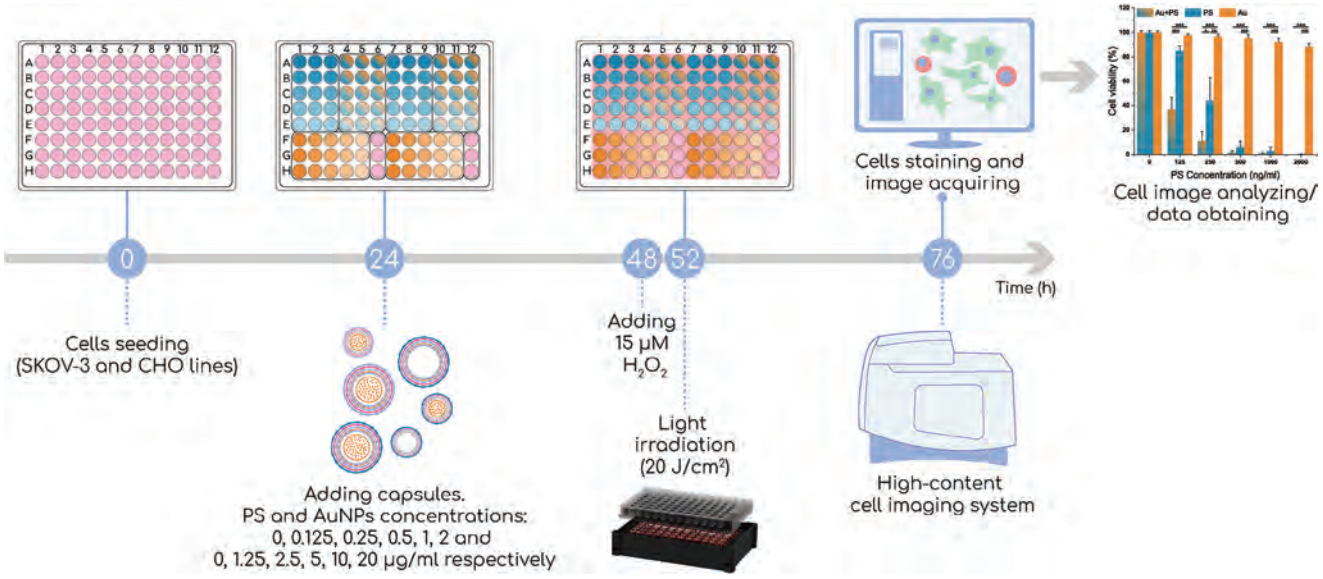

Figure 10. Cell experiment timeline.

USA). To calculate size distribution at least 100 gold nanoparticles were analyzed.

Nanoparticle Tracking Analysis: The concentration of the capsules was evaluated using the NanoSight NS300 (Malvern Instruments Ltd, UK). The analyzed samples were diluted 1000 to 2000 times. The camera level was set to 12 for light scatter mode. Data were analyzed using NTA 3.4 software (Malvern Instruments Ltd, UK).

XPS: The chemical state were analyzed by X-ray photoelectron spectroscopy (XPS), using a Theta Probe spectrometer under high-vacuum conditions (base pressure $<2 \times 10^{-9}$ mbar) with a monochromatic Al-Kα X-ray source (1486.6 eV). Photoelectron spectra were acquired using the fixed analyzer transmission mode at 50 eV pass energy.

LED Phototherapy Device: For irradiation of cells with red light, a custom phototherapy device was made. The device was designed to direct light to each well of the 96 Eppendorf well-plate. To achieve that, LEDs with a central emission wavelength of 658 nm (Figure S6c, Supporting Information) were placed directly under each of the 96 sample wells (Figure S6a, Supporting Information). The LED emission spectrum was measured using a ThorLabs spectrometer CCS200/M. The total light power delivered to each well was measured using a ThorLabs 121 C photodiode power sensor and amounted to 6.5 mW. The sensor aperture was circular with a diameter of 0.6 cm, giving a total power density of 23 mWcm−2 delivered to each well. The device was designed so that one can turn on all 96 LEDs, or only 48 LEDs (Figure S6b, Supporting Information). This was done to facilitate experiments that require control samples. Moreover, below the LEDs, a cooler was placed to prevent the LEDs from overheating.

Catalytic Experiments: In the presence of catalase, hydrogen peroxide decomposes to water and oxygen:

$$2H_2O_2 \rightarrow 2H_2O + O_2 \quad (5)$$

The catalase-like activity of gold nanoparticles of different sizes (3 and 30 nm) was evaluated based on the consumption of H_2O_2 in phosphate buffer solutions with different pH values. All reactions were carried out at 37 °C in glassware to avoid the adhesion of the nanoparticles to the plastic walls. 1 mL of 20 mM H_2O_2 was mixed with 900 μL of buffer with the desired pH and 100 μL of gold nanoparticles with a concentration of 0.3 mgmL^{-1}. The residual H_2O_2 was monitored at 240 nm using UV–vis spectroscopy (Tecan Infinite M Nano+, Tecan Trading AG, Männedorf, Switzerland) each hour during the first eight hours and after 24, 48, and 72 h after the reaction started. Moreover, control experiments were performed in the absence of a catalyst under the same conditions. On the basis of spectrometry data, kinetic curves were plotted, and the reaction rate was calculated for linear range and used further as the main parameter for nanozyme activity comparison. For further experiments, two pH values were chosen: 7.4 to mimic physiological conditions and 7.0 as closest to the environment of the cancer cell.[63–67]

Cell Cultures: Human ovarian adenocarcinoma, SKOV-3 cell line were used to represent cancer cells and Chinese hamster ovarian cell line, CHO were used to represent healthy cells, both were obtained from the American Tissue Type Collection (catalog numbers HTB-77 and CCL-61, respectively). Both cell lines were grown in RPMI 1640 Medium supplemented with 10% FBS and 1% Penicillin-Streptomycin, at 37 °C, in a 5% CO_2 humidified atmosphere. Although in most cases, especially in experiments involving receptors, the comparison of human and hamster cells was not legitimate, in this case the choice was based on their common epithelial ovarian origin and the difference in intracellular pH (pHi), since SKOV-3 cells have pHi around 7[44] and CHO around 7.4.[68]

Cell Experiment: The experiment timeline is shown in **Figure 10**. Briefly, both types of cells were seeded at two 96-well plates (Perkin Elmer LLC 6055302), one to keep it in the dark and one for experiments with light irradiation, and kept until 100% density was achieved. Thereafter, the culture medium was refreshed and different types of capsules or pure PS were added in decreasing concentrations to the cells. 24 h later, SKOV-3 cells were treated with 15 μM of H_2O_2 to simulate TME. 4 h after cells were irradiated with LED device, LD = 20 Jcm^{-2}. Cells were stained with three dyes: Calcein AM, cell-permeant dye (Invitrogen) to color living cells, Hoechst 33342 (Invitrogen) to color all cells nuclei, and propidium iodide (Invitrogen) used for staining dead cells nuclei. Operetta CLS High Content Analysis System (Perkin Elmer) was used to obtain fluorescent images from wells, and Harmony High-Content Imaging and Analysis Software (Perkin Elmer) was used to calculate the number of cells in the well. Cell viability was calculated using the following formula:

$$CV = \frac{\text{Number of alive cells in the well}}{\text{Mean number of alive cells in the control wells}} \quad (6)$$

Supporting Information

Supporting Information is available from the Wiley Online Library or from the author.

© 2024 Wiley-VCH GmbH

15214117, 2024, 5, Downloaded from https://onlinelibrary.wiley.com/doi/10.1002/ppsc.202300149 by ITMO University, Wiley Online Library on [17/07/2024]. See the Terms and Conditions (https://onlinelibrary.wiley.com/terms-and-conditions) on Wiley Online Library for rules of use; OA articles are governed by the applicable Creative Commons License

Acknowledgements

Zeta-potential and size measurements by DLS, fluorescent images by Operetta CLS High Content Analysis System were performed using the equipment of the "Bioimaging and Spectroscopy" Core Facility of the Skolkovo Institute of Science and Technology. Cryo-TEM and TEM analysis were performed as a part of work on topic Laser technologies for biomedical applications (no.122122600055–2), fluorescent imaging as part of RSF No. 21-79-10384. This work was supported by Clover Program: Joint Research Projects of Skoltech, MIPT, and ITMO.

Conflict of Interest

The authors declare no conflict of interest.

Data Availability Statement

The data that support the findings of this study are available from the corresponding author upon reasonable request.

Keywords

AuNPs, gold nanoparticles, nanozymes, PDT (photodynamic therapy), polymer capsules

Received: September 26, 2023
Revised: December 26, 2023
Published online: January 27, 2024

[1] L. Huang, S. Zhao, J. Wu, L. Yu, N. Singh, K. Yang, M. Lan, P. Wang, J. S. Kim, *Coord. Chem. Rev.* **2021**, *438*, 213888.
[2] R. Alzeibak, T. A. Mishchenko, N. Y. Shilyagina, I. V. Balalaeva, M. V. Vedunova, D. V. Krysko, *J. ImmunoTher. Cancer* **2021**, *9*, e001926.
[3] P. Agostinis, K. Berg, K. A. Cengel, T. H. Foster, A. W. Girotti, S. O. Gollnick, S. M. Hahn, M. R. Hamblin, A. Juzeniene, D. Kessel, M. Korbelik, J. Moan, P. Mroz, D. Nowis, J. Piette, B. C. Wilson, J. Golab, *Ca-Cancer J. Clin.* **2011**, *61*, 250.
[4] G. Yang, L. Xu, Y. Chao, J. Xu, X. Sun, Y. Wu, R. Peng, Z. Liu, *Nat. Commun.* **2017**, *8*, 902.
[5] Z. Ma, X. Jia, J. Bai, Y. Ruan, C. Wang, J. Li, M. Zhang, X. Jiang, *Adv. Funct. Mater.* **2017**, *27*, 1604258.
[6] Z. Gao, Y. Li, Y. Zhang, kaiwu Cheng, P. An, F. Chen, J. Chen, C. You, Q. Zhu, B. Sun, *ACS Appl. Mater. Interfaces* **2020**, *12*, 1963.
[7] P. Chelikani, I. Fita, P. C. Loewen, *Cell. Mol. Life Sci. (CMLS)* **2004**, *61*, 192.
[8] G. J. Burton, E. Jauniaux, *Best Pract. Res. Clin. Obstet. Gynaecol.* **2011**, *25*, 287.
[9] J. Lu, Y. Mao, S. Feng, X. Li, Y. Gao, Q. Zhao, S. Wang, *Acta Biomater.* **2022**, *148*, 310.
[10] Y. Huang, J. Ren, X. Qu, *Chem. Rev.* **2019**, *119*, 4357.
[11] J. Mujtaba, J. Liu, K. K. Dey, T. Li, R. Chakraborty, K. Xu, D. Makarov, R. A. Barmin, D. A. Gorin, V. P. Tolstoy, G. Huang, A. A. Solovev, Y. Mei, *Adv. Mater.* **2021**, *33*, 2007465.
[12] Y. Hu, H. Cheng, X. Zhao, J. Wu, F. Muhammad, S. Lin, J. He, L. Zhou, C. Zhang, Y. Deng, P. Wang, Z. Zhou, S. Nie, H. Wei, *ACS Nano* **2017**, *11*, 5558.
[13] Y. Song, K. Qu, C. Zhao, J. Ren, X. Qu, *Adv. Mater.* **2010**, *22*, 2206.
[14] Y. Sang, F. Cao, W. Li, L. Zhang, Y. You, Q. Deng, K. Dong, J. Ren, X. Qu, *J. Am. Chem. Soc.* **2020**, *142*, 5177.
[15] T. Teranishi, *C. R. Chim.* **2003**, *6*, 979.
[16] X. Huang, M. A. El-Sayed, *J. Adv. Res.* **2010**, *1*, 13.
[17] X. Zhou, W. Xu, G. Liu, D. Panda, P. Chen, *J. Am. Chem. Soc.* **2010**, *132*, 138.
[18] R. Seoudi, D. A. Said, *World J. Nano Sci. Eng.* **2011**, *01*, 51.
[19] N. Lopez, J. K. Nørskov, *J. Am. Chem. Soc.* **2002**, *124*, 11262.
[20] C.-P. Liu, T.-H. Wu, C.-Y. Liu, K.-C. Chen, Y.-X. Chen, G.-S. Chen, S.-Y. Lin, *Small* **2017**, *13*, 1700278.
[21] M. Drozd, M. Pietrzak, P. G. Parzuchowski, E. Malinowska, *Anal. Bioanal. Chem.* **2016**, *408*, 8505.
[22] W. He, Y.-T. Zhou, W. G. Wamer, X. Hu, X. Wu, Z. Zheng, M. D. Boudreau, J.-J. Yin, *Biomaterials* **2013**, *34*, 765.
[23] J. Li, W. Liu, X. Wu, X. Gao, *Biomaterials* **2015**, *48*, 37.
[24] T. Kiyonaga, Q. Jin, H. Kobayashi, H. Tada, *ChemPhysChem* **2009**, *10*, 2935.
[25] Z. Zhu, Z. Guan, S. Jia, Z. Lei, S. Lin, H. Zhang, Y. Ma, Z.-Q. Tian, C. J. Yang, *Angew. Chem., Int. Ed.* **2014**, *53*, 12503.
[26] L. Guerrini, R. Alvarez-Puebla, N. Pazos-Perez, *Materials* **2018**, *11*, 1154.
[27] C. D. Walkey, W. C. W. Chan, *Chem. Soc. Rev.* **2012**, *41*, 2780.
[28] B. D. Johnston, W. G. Kreyling, C. Pfeiffer, M. Schäffler, H. Sarioglu, S. Ristig, S. Hirn, N. Haberl, S. Thalhammer, S. M. Hauck, M. Semmler–Behnke, M. Epple, J. Hühn, P. D. Pino, W. J. Parak, *Adv. Funct. Mater.* **2017**, *27*, 1701956.
[29] M. R. K. Ali, Y. Wu, M. A. El-Sayed, *J. Phys. Chem. C* **2019**, *123*, 15375.
[30] Y. Que, C. Feng, S. Zhang, X. Huang, *J. Phys. Chem. C* **2015**, *119*, 1960.
[31] X. Meng, I. Zare, X. Yan, K. Fan, *WIREs Nanomedicine and Nanobiotechnology* **2020**, *12*, e1602.
[32] P. Suchomel, L. Kvitek, R. Prucek, A. Panacek, A. Halder, S. Vajda, R. Zboril, *Sci. Rep.* **2018**, *8*, 4589.
[33] V. Sokolova, J. Ebel, S. Kollenda, K. Klein, B. Kruse, C. Veltkamp, C. M. Lange, A. M. Westendorf, M. Epple, *Small* **2022**, *18*, 2201167.
[34] A. Sani, C. Cao, D. Cui, *Biochem. Biophys. Rep.* **2021**, *26*, 100991.
[35] W. G. Kreyling, A. M. Abdelmonem, Z. Ali, F. Alves, M. Geiser, N. Haberl, R. Hartmann, S. Hirn, D. J. de Aberasturi, K. Kantner, G. Khadem-Saba, J.-M. Montenegro, J. Rejman, T. Rojo, I. R. de Larramendi, R. Ufartes, A. Wenk, W. J. Parak, *Nat. Nanotechnol.* **2015**, *10*, 619.
[36] N. Khlebtsov, L. Dykman, *Chem. Soc. Rev.* **2011**, *40*, 1647.
[37] C. Kirchner, A. M. Javier, A. Susha, A. Rogach, O. Kreft, G. Sukhorukov, W. Parak, *Talanta* **2005**, *67*, 486.
[38] A. Biswas, L. R. Bornhoeft, S. Banerjee, Y.-H. You, M. J. McShane, *ACS Sens.* **2017**, *2*, 1584.
[39] G. Schneider, G. Decher, *Langmuir* **2008**, *24*, 1778.
[40] M. V. Novoselova, S. V. German, T. O. Abakumova, S. V. Perevoschikov, O. V. Sergeeva, M. V. Nesterchuk, O. I. Efimova, K. S. Petrov, V. S. Chernyshev, T. S. Zatsepin, D. A. Gorin, *Colloids Surf., B* **2021**, *200*, 111576.
[41] L. J. De Cock, S. De Koker, B. G. De Geest, J. Grooten, C. Vervaet, J. P. Remon, G. B. Sukhorukov, M. N. Antipina, *Angew. Chem., Int. Ed.* **2010**, *49*, 6954.
[42] A. Larrañaga, I. L. M. Isa, V. Patil, S. Thamboo, M. Lomora, M. A. Fernández-Yague, J.-R. Sarasua, C. G. Palivan, A. Pandit, *Acta Biomater.* **2018**, *67*, 21.
[43] A. L. Popov, N. Popova, D. J. Gould, A. B. Shcherbakov, G. B. Sukhorukov, V. K. Ivanov, *ACS Appl. Mater. Interfaces* **2018**, *10*, 14367.
[44] Y.-S. Liu, Y. Sun, P. T. Vernier, C.-H. Liang, S. Y. C. Chong, M. A. Gundersen, *J. Phys. Chem. C* **2007**, *111*, 2872.
[45] Y. Liu, F. A. Villamena, J. L. Zweier, *Chem. Commun.* **2008**, 4336.
[46] M. C. Krishna, S. English, K. Yamada, J. Yoo, R. Murugesan, N. Devasahayam, J. A. Cook, K. Golman, J. H. Ardenkjaer-Larsen, S. Subramanian, J. B. Mitchell, *Proc. Natl. Acad. Sci.* **2002**, *99*, 2216.
[47] Y. Takakusagi, R. Kobayashi, K. Saito, S. Kishimoto, M. C. Krishna, R. Murugesan, K. ichiro Matsumoto, *Metabolites* **2023**, *13*, 69.
[48] C. Rizzi, *Free Radical Biol. Med.* **2003**, *35*, 1608.

 © 2024 Wiley-VCH GmbH

15214117, 2024, 5, Downloaded from https://onlinelibrary.wiley.com/doi/10.1002/ppsc.202300149 by ITMO University, Wiley Online Library on [17/07/2024]. See the Terms and Conditions (https://onlinelibrary.wiley.com/terms-and-conditions) on Wiley Online Library for rules of use; OA articles are governed by the applicable Creative Commons License

[49] I. Dhimitruka, M. Velayutham, A. A. Bobko, V. V. Khramtsov, F. A. Villamena, C. M. Hadad, J. L. Zweier, *Bioorg. Med. Chem. Lett.* **2007**, *17*, 6801.
[50] K. Palewska, J. Sworakowski, J. Lipiński, *Opt. Mater.* **2012**, *34*, 1717.
[51] I. V. Martynenko, A. O. Orlova, V. G. Maslov, A. V. Fedorov, K. Berwick, A. V. Baranov, *Beilstein J. Nanotechnol.* **2016**, *7*, 1018.
[52] C. P. Gulka, A. C. Wong, D. W. Wright, *Chem. Commun.* **2016**, *52*, 1266.
[53] T. Wang, D. Xiao, *Microchim. Acta* **2021**, *188*, 193.
[54] A. A. Antipov, G. B. Sukhorukov, *Adv. Colloid Interface Sci.* **2004**, *111*, 49.
[55] J. Gubicza, J. L. Labar, L. M. Quynh, N. H. Nam, N. H. Luong, *Mater. Chem. Phys.* **2013**, *138*, 449.
[56] E. Jang, E.-K. Lim, J. Choi, J. Park, Y.-J. Huh, J.-S. Suh, Y.-M. Huh, S. Haam, *Cryst. Growth Des.* **2012**, *12*, 37.
[57] E. Sokolova, A. Senatskaya, S. Lermontova, E. Akinchits, L. Klapshina, A. Brilkina, I. Balalaeva, *Sovrem Tekhnologii Med.* **2020**, *12*, 34.
[58] D. G. Duff, A. Baiker, P. P. Edwards, *Langmuir* **1993**, *9*, 2301.
[59] R. E. Noskov, A. Machnev, I. I. Shishkin, M. V. Novoselova, A. V. Gayer, A. A. Ezhov, E. A. Shirshin, S. V. German, I. D. Rukhlenko, S. Fleming, B. N. Khlebtsov, D. A. Gorin, P. Ginzburg, *Adv. Mater.* **2021**, *33*, 2008484.
[60] D. B. Trushina, T. V. Bukreeva, M. N. Antipina, *Cryst. Growth Des.* **2016**, *16*, 1311.
[61] H. Bahrom, A. A. Goncharenko, L. I. Fatkhutdinova, O. O. Peltek, A. R. Muslimov, O. Y. Koval, I. E. Eliseev, A. Manchev, D. Gorin, I. I. Shishkin, R. E. Noskov, A. S. Timin, P. Ginzburg, M. V. Zyuzin, *ACS Sustainable Chem. Eng.* **2019**, *7*, 19142.
[62] S. V. German, M. V. Novoselova, D. N. Bratashov, P. A. Demina, V. S. Atkin, D. V. Voronin, B. N. Khlebtsov, B. V. Parakhonskiy, G. B. Sukhorukov, D. A. Gorin, *Sci. Rep.* **2018**, *8*, 17763.
[63] S. Simon, D. Roy, M. Schindler, *Proc. Natl. Acad. Sci.* **1994**, *91*, 1128.
[64] O. Warburg, F. Wind, E. Negelein, *J. Gen. Physiol.* **1927**, *8*, 519.
[65] J. Griffiths, *Br. J. Cancer* **1991**, *64*, 425.
[66] B. A. Webb, M. Chimenti, M. P. Jacobson, D. L. Barber, *Nat. Rev. Cancer* **2011**, *11*, 671.
[67] I. F. Tannock, D. Rotin, *Cancer Res.* **1989**, *49*, 4373.
[68] P. Ozkan, R. Mutharasan, *Biochim. Biophys. Acta, Gen. Subj.* **2002**, *1572*, 143.

© 2024 Wiley-VCH GmbH

15214117, 2024, 5, Downloaded from https://onlinelibrary.wiley.com/doi/10.1002/ppsc.202300149 by ITMO University, Wiley Online Library on [17/07/2024]. See the Terms and Conditions (https://onlinelibrary.wiley.com/terms-and-conditions) on Wiley Online Library for rules of use; OA articles are governed by the applicable Creative Commons License